Supporting Information for

Identification of Protein-Bound Dinitrosyl Iron Complexes by Nuclear Resonance Vibrational Spectroscopy

Zachary J. Tonzetich,[†] Hongxin Wang,[‡] Devrani Mitra,[||] Christine E. Tinberg,[†] Loi H. Do,[†] Francis E. Jenney, Jr.,[§] Michael W. W. Adams,[#] Stephen P. Cramer,[*,||,‡] and Stephen J. Lippard[*,†]

[†]*Department of Chemistry, Massachusetts Institute of Technology, Cambridge, MA 02139*
[||]*Department of Applied Science, University of California, Davis, CA 95616*
[‡]*Physical Biosciences Division, Lawrence Berkeley National Laboratory, Berkeley, CA 94720*
[§]*GA Campus - Philadelphia College of Osteopathic Medicine, Suwanee, GA 30024*
[#]*Department of Biochemistry and Molecular Biology, University of Georgia, Athens, GA 30602*

RECEIVED DATE (automatically inserted by publisher); spjcramer@lbl.gov, lippard@mit.edu

Contents:

Experimental Details S2-S5

Supplementary Tables and Figures S6-S25

Table S1. Crystallographic data and refinement details for RRE and rRRE S6
Table S2. Comparison of ^{57}Fe MB parameters for DNIC, RRE, and rRRE S7

Figure S1. Synthetic scheme for ^{57}Fe-labeled model compounds S8
Figure S2. IR spectrum of $(Et_4N)[^{57}Fe(NO)_2(SPh)_2]$ S9
Figure S3. EPR spectrum of $(Et_4N)[^{57}Fe(NO)_2(SPh)_2]$ S9
Figure S4. IR spectrum of $(Et_4N)[^{57}Fe(^{15}NO)_2(SPh)_2]$ S10
Figure S5. EPR spectrum of $(Et_4N)[^{57}Fe(^{15}NO)_2(SPh)_2]$ S10
Figure S6. IR spectrum of $[^{57}Fe_2(\mu\text{-}SPh)_2(NO)_4]$ S11
Figure S7. IR spectrum of $[^{57}Fe_2(\mu\text{-}SPh)_2(^{15}NO)_4]$ S11
Figure S8. Thermal ellipsoid drawing of $[Fe_2(\mu\text{-}SPh)_2(NO)_4]$ S12
Figure S9. IR spectrum of $(Et_4N)[^{57}Fe_2(\mu\text{-}SPh)_2(NO)_4]$ S13
Figure S10. EPR spectrum of $(Et_4N)[Fe_2(\mu\text{-}SPh)_2(NO)_4]$ S13
Figure S11. UV-vis spectrum of $(Et_4N)[Fe_2(\mu\text{-}SPh)_2(NO)_4]$ S14
Figure S12. Mössbauer spectrum of $(Et_4N)[Fe_2(\mu\text{-}SPh)_2(NO)_4]$ S14
Figure S13. EPR spectral changes associated with rRRE to DNIC conversion S15
Figure S14. Thermal ellipsoid drawing of $(Et_4N)[Fe_2(\mu\text{-}SPh)_2(NO)_4]$ S15
Figure S15. IR spectrum of $(Et_4N)[^{57}Fe_4(\mu_3\text{-}S)_3(NO)_7]$ S16
Figure S16. IR spectrum of $(Et_4N)[^{57}Fe_4(\mu_3\text{-}S)_3(^{15}NO)_7]$ S16
Figure S17. NRVS spectra of $[^{57}Fe_2(\mu\text{-}SPh)_2(^{14/15}NO)_4]$ S17
Figure S18. NRVS spectrum of $(Et_4N)[^{57}Fe_2(\mu\text{-}SPh)_2(NO)_4]$ S17
Figure S19. NRVS spectra of $(Et_4N)[^{57}Fe_4(\mu_3\text{-}S)_3(^{14/15}NO)_7]$ S18
Figure S20. Overlay of NRVS spectra for DNIC, RRE, RBS, and rRRE S18
Figure S21. Calculated NRVS spectra for $(Et_4N)[^{57}Fe(^{14/15}NO)_2(SPh)_2]$ S19
Figure S22. Calculated NRVS spectra for $[^{57}Fe_2(\mu\text{-}SPh)_2(^{14/15}NO)_4]$ S20
Figure S23. Calculated NRVS spectra for $(Et_4N)[^{57}Fe_2(\mu\text{-}SPh)_2(^{14}NO)_4]$ S21
Figure S24. Calculated NRVS spectra of $(Et_4N)[^{57}Fe_4(\mu_3\text{-}S)_3(^{14/15}NO)_7]$ S22
Figure S25. Overlay of ^{57}Fe MB fits for DNIC, RRE, and rRRE S23
Figure S26. Structure of *P. furiosus* Fd D14C S24
Figure S27. EPR spectrum of PAPA NONOate treated *P. furiosus* Fd D14C S24
Figure S28. Comparison of NRVS spectra for Fd D14C, NO treated Fd, and RBS S25

References S26

Experimental Details

General Comments. Manipulations of air- and moisture-sensitive materials were performed under an atmosphere of nitrogen gas using standard Schlenk techniques or in an MBraun glovebox under an atmosphere of purified nitrogen. Acetonitrile, tetrahydrofuran, and diethyl ether were purified by passage through activated alumina then stored over 4-Å molecular sieves prior to use.[1] Methanol was distilled from magnesium turnings under an argon atmosphere and stored over 4-Å molecular sieves prior to use. Nitric oxide (Airgas, 99%) was purified by a method adapted from the literature.[2] The NO gas stream was passed through an Ascarite column (NaOH fused on silica gel) and a 6-ft coil filled with silica gel cooled to −78 °C. ^{15}N nitric oxide (Cambridge Isotope Labs) was purified in similar fashion except for passage through the silica gel coil. $^{14/15}$NO gas was stored and transferred under an inert atmosphere using standard gas storage bulbs and gas-tight syringes, respectively.

Physical Measurements. FT-IR spectra were recorded with a ThermoNicolet Avatar 360 spectrophotometer running the OMNIC software. Solid samples were pressed into KBr disks and solution samples were prepared in an air-tight Graseby-Specac solution cell with CaF_2 windows and 0.1 mm spacers. UV−vis spectra were recorded on a Cary-50 spectrophotometer in air-tight Teflon-capped quartz cells. Samples for ^{57}Fe Mössbauer studies were prepared by grinding a solid sample with Apiezon-N grease. Samples were placed in a 90 K cryostat during measurement. A ^{57}Co/Rh source was moved at a constant acceleration at room temperature against the absorber sample. All isomer shift (δ) and quadrupole splitting (ΔE_Q) values are reported with respect to ^{57}Fe-enriched metallic iron foil that was used for velocity calibration. The displayed spectra were folded to enhance the signal-to-noise ratios. Fits of the data were calculated by the WMOSS version 2.5 plot and fit program.[3] X-band EPR spectra were recorded on a Bruker EMX EPR spectrometer. Temperature control was maintained with a quartz finger dewar (77 K). Spectra were recorded in 4 mm o.d. quartz EPR tubes capped with a tight-fitting rubber septum.

Materials. ^{57}Fe and HSPh were obtained from commercial suppliers and used as received. $(Et_4N)_2[^{57}Fe_4(SPh)_{10}]$ and $(Et_4N)[^{57}Fe_4(\mu_3\text{-}S)_4(SPh)_4]$ were prepared by slight modification of a literature procedure[4] starting from $^{57}Fe(OTf)_2{\cdot}2CH_3CN$[5] (Figure S1). PAPA NONOate (propylamine propylamine NONOate, CAS 146672-58-4) was purchased from Cayman chemicals and used as received.

Preparation of $(Et_4N)[^{57}Fe(NO)_2(SPh)_2]$ and $[^{57}Fe_2(\mu\text{-}SPh)_2(NO)_4]$. To 0.146 g (92.4 μmol) of $(Et_4N)_2[^{57}Fe_4(SPh)_{10}]$ in 8 mL of CH_3CN was added 20.0 mL (770 μmol) of NO gas by syringe. The solution immediately changed from golden brown to deep red. The reaction was allowed to stir at 25 ºC for 2.5 h, during which time a red precipitate formed. The precipitate was isolated by filtration, washed with CH_3CN, and dried in vacuo to afford 0.0322 g of $[^{57}Fe_2(\mu\text{-}SPh)_2(NO)_4]$ as a red solid (77% yield). The remaining filtrate was evaporated to dryness and the resulting residue extracted into THF. After filtration, the THF solution was concentrated in vacuo to 3 mL and set aside at −30 ºC for 24 h. During this time red needles deposited in the crystallization vial. The crystals were isolated by decanting the mother liquor and washed with Et_2O to give 0.0343 g of $(Et_4N)[^{57}Fe(NO)_2(SPh)_2]$ (40% yield). The identity of each compound was confirmed by UV-vis, IR, EPR (for $(Et_4N)[^{57}Fe(NO)_2(SPh)_2]$), and NMR (for $[^{57}Fe_2(\mu\text{-}$

$SPh)_2(NO)_4]$) spectroscopy, which matched values previously published[6,7] for the ^{56}Fe compounds. ^{15}N-Labeled compounds were prepared in an analogous fashion by employing ^{15}NO gas. Selected IR and EPR spectra are displayed in Figures S2-S7. The solid-state structure of $[Fe_2(\mu\text{-}SPh)_2(NO)_4]$ is displayed in Figure S8 (see also Table S1).

Synthesis of $(Et_4N)[Fe_2(\mu\text{-}SPh)_2(NO)_4]$. To 0.0746 g (166 μmol) of $[Fe_2(\mu\text{-}SPh)_2(NO)_4]$ in 15 mL of THF was added 0.0861 g (187 μmol) of 5% Na/Hg. The solution was allowed to stir vigorously at 25 ºC for 20 h, during which time the solution changed from red to dark green. To the green solution was added a solution of Et_4NCl (0.0364 g, 220 μmol) in 4 mL of CH_3CN. The mixture was allowed to stir for an additional 2 h. All volatiles were removed in vacuo and the residue was extracted into 10 mL of THF. The THF solution was decanted away from the mercury and filtered through glass filter paper. The resulting green solution was concentrated in vacuo to ~3 mL. After layering with an equal volume of Et_2O, the mixture was allowed to stand at −30 ºC for 24 h, during which time green needles deposited. The needles were washed with Et_2O and dried in vacuo to give 0.0689 g (72% yield). Samples of $(Et_4N)[Fe_2(\mu\text{-}SPh)_2(NO)_4]$ were contaminated with 5–10% of $(Et_4N)[Fe(NO)_2(SPh)_2]$ due to spontaneous interconversion in solution (vida infra, Figure S13).[8] Repeated crystallization from THF/Et_2O produced material of sufficient purity for NRVS and Mössbauer studies, although a satisfactory elemental analysis could not be obtained. IR (KBr, cm^{-1}): 2918, 2850, 1685 (ν_{NO}), 1648 (ν_{NO}), 1574, 1474, 1450, 1436, 1394, 794, 692, 480; (CH_3CN, cm^{-1}): 1687 (ν_{NO}), 1672 (ν_{NO}). UV-vis (THF) λ_{max}, nm (ε, $M^{-1}cm^{-1}$): 370 (6500), 452 (4000), 656 (1800), 970 (2300). EPR (X-band, 2-MeTHF): 77 K $g_\perp$ = 2.01, $g_\parallel$ = 1.97; 293 K g_{iso} = 1.99. ^{57}Fe Mössbauer: δ = 0.23(2) mm/s, ΔE_Q = 0.35(2) mm/s, Γ = 0.30(2) mm/s. Representative anal. Calcd for $C_{20}H_{30}Fe_2N_5O_4S_2$: C, 41.39; H, 5.21; N, 12.07. Found C, 44.16; H, 5.42; N, 11.01. The ^{57}Fe analog was prepared in an identical fashion starting from $[^{57}Fe_2(\mu\text{-}SPh)_2(NO)_4]$. For spectroscopic data see Figures S9-S12. The solid-state structure of $(Et_4N)[Fe_2(\mu\text{-}SPh)_2(NO)_4]$ is displayed in Figure S14 (see also Table S1).

Preparation of $(Et_4N)[^{57}Fe_4(\mu_3\text{-}S)_3(NO)_7]$. This compound was prepared according to a published procedure for the ^{56}Fe analog.[6] Briefly, to 0.200 g (190 μmol) of $(Et_4N)_2[^{57}Fe_4(\mu_3\text{-}S)_4(SPh)_4]$ in 10 mL of CH_3CN was added 30.0 mL (1.2 mmol) of NO gas by syringe. The mixture was allowed to stir at ambient temperature for 3 h during which time it changed from dark red to brown. All volatiles were removed under reduced pressure, and the resulting residue was washed thoroughly with Et_2O. The residue was then extracted into 10 mL of THF and filtered to remove un-reacted starting material. The THF solution was layered with 3 mL of pentane and set aside at -30 ºC for 24 h. During this time black crystals deposited in the crystallization vial. The crystals were isolated by decanting the mother liquor and washed with pentane to give 0.0371 g of $(Et_4N)[^{57}Fe_4(\mu_3\text{-}S)_3(NO)_7]$ (30% yield). The identity of the compound was confirmed by IR spectroscopy, which matched values previously published for the ^{56}Fe compound.[6,9] The ^{15}N-labeled compound was prepared in an analogous fashion by employing ^{15}NO gas. The IR spectra for each isotopomer are displayed in Figures S15 and S16.

***Pyrococcus furiousus* Fd D14C.** Recombinant *Pyrococcus furiosus* ferredoxin (D14C mutant) was expressed and purified using the same expression vector and conditions previously described.[8] For preparation of protein with ^{57}Fe substituted $\{Fe_4S_4\}$ cores, the protein was reconstituted in a manner similar to that as described.[9] The protein (50 mg, ~7.6 μmol) was first denatured by addition of HCl (1.2 M), EDTA (0.5 M), and 2-mercaptoethanol (2-ME) (0.2 M).

The sample was incubated slowly swirling at 37 ºC for 4 hours resulting in precipitation and loss of the brown color. The protein was pelleted by centrifugation at 18,000 × *g* and resuspended in buffer A (0.5 M Tris pH 8.0) with 0.5 M 2-ME and this precipitation was repeated twice. The final (white) pellet was washed first by resuspending in 10 mL ice cold 100% acetone and centrifuging again, then briefly with HPLC grade water, and dried. The pellet was dissolved in buffer A with 100 mM 2-ME to a concentration of ~ 5 mg/ml protein. For the iron, 8.6 mg of elemental ^{57}Fe (95%) was dissolved in 80 µl of aqua regia (3:1 HCl:HNO_3) resulting in a completely dissolved, bright yellow solution, to which ~80 µl of 5 M NaOH was added to slightly neutralize the solution. The solubilized protein was diluted to ~2 mg/ml with buffer A while stirring under Ar, and 152 µmoles (20 fold excess) of Na_2S in buffer A was injected, followed by the ^{57}Fe (152 µmol, a 20 fold molar excess over the protein), and the solution stirred overnight at room temperature under Ar. The next day, the reconstituted protein was diluted 1:1 with water, filtered through a 0.45 micron syringe filter to remove precipitated iron, and loaded onto a DEAE-FF anion exchange column (GE Healthcare, Piscataway, NJ) equilibrated in buffer B (50 mM Tris pH 8.0), block eluted with 500 mM NaCl in buffer B, and concentrated/buffer exchanged into buffer B by ultrafiltration with Amicon Ultra-4 5 kDa NMWL filters (Millipore, Billerica, MA). The concentrated protein was flash-frozen in liquid N_2.

NRVS Data Acquisition. For NRVS measurements, samples were loaded into 3 × 7 × 1 mm^3 (interior dimensions) Lucite cuvettes. ^{57}Fe NRVS spectra were recorded using published procedures[10] on multiple occasions at beamline 9-XU at SPring-8, Japan, and beamline 18 at ESRF, France. Fluxes were on the order of 1-3 × 10^9 photons/sec in a 1.2 eV bandpass. During NRVS measurements, samples were maintained at low temperatures using liquid He cryostats (head temperature < 10 K). The real sample temperatures were calculated from the ratio of anti-Stokes to Stokes intensity by the expression $S(-E) = S(E)e^{(-E/kT)}$ and were obtained at 35-50 K. Nuclear fluorescence and delayed Fe *K* fluorescence were recorded with an APD array at both beamlines. Each scan took about 50 min, and all scans were added and normalized to the intensity of the incident beam. Each final model compound spectrum represents 3 hours of data collections, whereas the *P. furiosus* Fd D14C protein + PAPA NONOate spectrum was measured for 16 h. Spectra were recorded between -200 to 800 cm^{-1}.

Empirical Force Field Normal Mode Analysis. Empirical normal mode calculations were conducted using the program 'Vibratz',[11,12] which uses the Urey-Bradley force field. The normal mode calculations for all the Fe-NO complexes started at higher symmetry, namely, C_{2v} for $(Et_4N)[^{57}Fe(^{14/15}NO)_2(SPh)_2]$ and C_{2h} for $[^{57}Fe_2(\mu\text{-}SPh)_2(^{14/15}NO)_4]$ and $(Et_4N)[^{57}Fe_2(\mu\text{-}SPh)_2(^{14}NO)_4]$), which was then relaxed to C_1 for the final computations. Initial estimates of the Fe–N and N–O force constants were taken from literature values for $[Fe(NO)_2(SPh)_2]^-$, which emphasized $Fe(NO)_2$ core vibration.[13] For the higher symmetry calculations, our simulations included the $Fe(SC)_2(NO)_2$ as a C_{2v} model for $(Et_4N)[^{57}Fe(^{14/15}NO)_2(SPh)_2]$ and $Fe_2S_2(NO)_4$ as C_{2h} models for $[^{57}Fe_2(\mu\text{-}SPh)_2(^{14/15}NO)_4]$ and $(Et_4N)[^{57}Fe_2(\mu\text{-}SPh)_2(^{14}NO)_4]$, respectively. The overall correlation between calculated and experimental spectra are satisfactory. The higher wavenumber regions are well reproduced in all the cases, although the lower wavenumber regions were better fit with relaxation of symmetry and inclusion of a larger number of atoms.

X-ray Data Collection and Structure Solution Refinement. Dark red needles of $[Fe_2(\mu\text{-}SPh)_2(NO)_4]$ were grown anaerobically by vapor diffusion of pentane into a saturated THF

solution at 25 ºC. Suitable crystals were mounted in Paratone N oil and frozen under a 110 K nitrogen cold stream maintained by a KRYO-FLEX low-temperature apparatus. Data were collected on a Bruker APEX CCD X-ray diffractometer with Mo Kα radiation (λ = 0.71073 Å) controlled by the SAINT software package.[14] Empirical absorption corrections were applied with SADABS[15] and the structure was checked for higher symmetry and twinning by the PLATON software.[16] The structure was solved by Patterson methods with refinement by full-matrix least-squares based on F^2 using SHELXTL-97.[17] Refinement of the structure as a pseudo-merohedral twin revealed a 55:45 occupancy of two domains. All non-hydrogen atoms were located and their positions refined anisotropically. Hydrogen atoms were assigned to idealized positions and given thermal parameters equal to either 1.5 (methyl hydrogen atoms) or 1.2 (non-methyl hydrogen atoms) times the thermal parameters of the atoms to which they were attached.

Green cubes of $(Et_4N)[Fe_2(\mu\text{-}SPh)_2(NO)_4]$ were grown by vapor diffusion of diethyl ether into a saturated THF solution at 25 ºC. A suitable crystal was mounted and data were collected and processed as described above. The $(Et_4N)[Fe_2(\mu\text{-}SPh)_2(NO)_4]$ molecule is located on a special position. Positional disorder of the tetraethylammonium cation was modeled in two different orientations with 50% occupancy by suppressing generation of special position constraints. Bonds to symmetry related atoms of the tetraethylammonium cation are excluded from the connectivity table. Treatment of hydrogen and non-hydrogen atoms was performed as described above.

Reaction of PAPA NONOate with *Pyrococcus furiosus* Ferredoxin D14C. In an anaerobic atmosphere, 200 μL of 4.6 mM *P. furiosus* Fd D14C mM (oxidized form, $\{Fe_4S_4\}^{2+}$) in 50 mM Tris pH 8.0 was treated with 40 μL of 190 mM PAPA NONOate in 50 mM Tris pH 8.0. The final protein concentration was 3.8 mM and that of PAPA NONOate was 32 mM (8.4 equiv). The reaction was incubated at 25 ºC for 120 min, then loaded into two NRVS cells and frozen in liquid nitrogen. The cells were stored at −80 ºC for 3 days prior to shipping. An aliquot of the reaction solution was diluted fivefold and used for EPR spectroscopy (Figure S27).

Supplementary Figures and Tables

Table S1. Crystallographic data and refinement parameters for $[Fe_2(\mu\text{-}SPh)_2(NO)_4]$ (**RRE**) and (Et_4N) $[Fe_2(\mu\text{-}SPh)_2(NO)_4]$ (**rRRE**).

Compound	**RRE**	**rRRE**
Empirical formula	$C_{12}H_{10}Fe_2N_4O_4S_2$	$C_{20}H_{30}Fe_2N_5O_4S_2$
Formula weight (g/mol)	450.06	580.31
Temperature (K)	110(2)	100(2)
Wavelength (Å)	0.71073	0.71073
Crystal system	Monoclinic	Monoclinic
Space group	$P2_1/c$	$P2_1/n$
Unit cell dimensions	a = 10.6409(9) Å	a = 8.1729(13) Å
	b = 10.9163(9) Å	b = 10.0823(17) Å
	c = 7.4015(6) Å	c = 15.840(3) Å
	β = 110.3110(10)°	β = 94.989(3)º
Volume ($Å^3$)	806.30(12)	1300.3(4)
Z	2	2
Calculated density (g/cm^3)	1.854	1.482
Absorption coefficient (mm^{-1})	2.083	1.311
F(000)	452	602
Crystal size	0.29 × 0.12 × 0.10	0.47 × 0.33 × 0.16
Θ range for data collection	1.87 to 28.30°	2.40 to 30.20°
Index ranges	$-14 \le h \le 14$,	$-11 \le h \le 11$,
	$-13 \le k \le 14$,	$-14 \le k \le 14$,
	$-9 \le l \le 9$	$-22 \le l \le 22$
Reflections collected	16524	27404
Independent reflections	2005 [R(int) = 0.0249]	3857 [R(int) = 0.0393]
Completeness to Θ	100.0 %	99.5 %
Absorption correction	Empirical	Empirical
Max. and min. transmission	0.8188 and 0.5834	0.8177 and 0.5779
Refinement method	Full-matrix least-squares on F^2	Full-matrix least-squares on F^2
Data / restraints / parameters	2005 / 0 / 110	3857 / 6 / 187
Goodness-of-fit on F^2	1.155	1.071
Final R indices [$I > 2\sigma(I)$]	R1 = 0.0148, wR2 = 0.0398	R1 = 0.0343, wR2 = 0.0679
R indices (all data)	R1 = 0.0150, wR2 = 0.0399	R1 = 0.0486, wR2 = 0.0736
Largest diff. peak and hole ($e \cdot Å^3$)	0.355 and -0.173	0.533 and -0.493

Table S2. Comparison of ^{57}Fe Mössbauer parameters for $(Et_4N)[Fe(NO)_2(SPh)_2]$ (**DNIC**), $[Fe_2(\mu\text{-}SPh)_2(NO)_4]$ (**RRE**), $(Et_4N)[Fe_4(\mu_3\text{-}S)_3(NO)_7]$ (**RBS**) and $(Et_4N)[Fe_2(\mu\text{-}SPh)_2(NO)_4]$ (**rRRE**). All data were recorded at 90 K in the absence of an applied magnetic field.

Compound	Isomer Shift, δ (mm/s)	Quadrupole Splitting, ΔE_Q (mm/s)	Linewidth, Γ (mm/s)
$(Et_4N)[Fe(NO)_2(SPh)_2]$	0.17(2)	0.68(2)	0.26(2)
$[Fe_2(\mu\text{-}SPh)_2(NO)_4]$	0.15(2)	0.97(2)	0.29(2)
$(Et_4N)[Fe_4(\mu_3\text{-}S)_3(NO)_7]$	0.15(2)*	0.81(2)	0.32(2)
$(Et_4N)[Fe_2(\mu\text{-}SPh)_2(NO)_4]$	0.23(2)	0.35(2)	0.30(2)

*Fit to a single site. See references 18 and 19 for a discussion of the Mössbauer spectrum of Roussin's black salt.

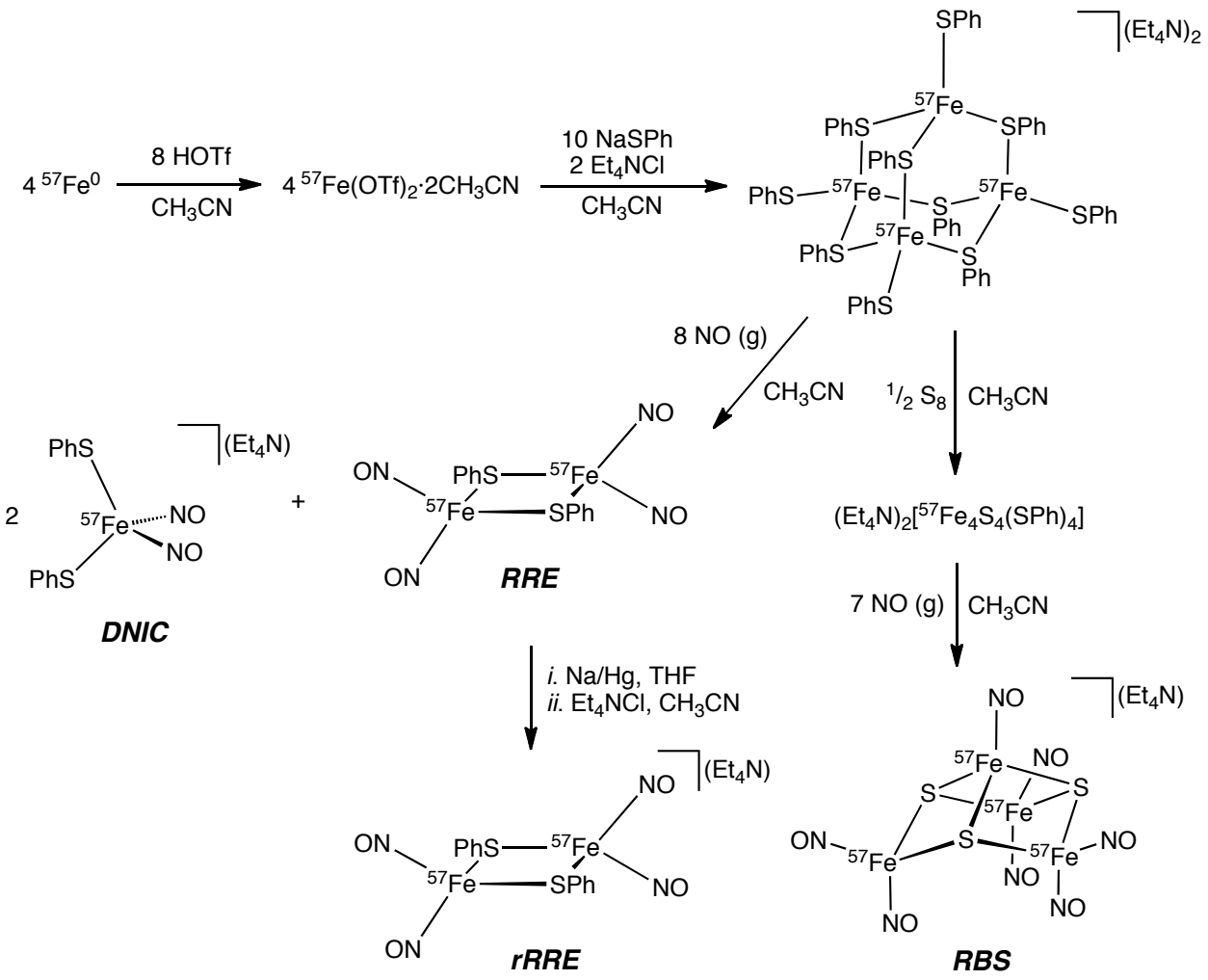

Figure S1. Synthetic scheme for preparation of ^{57}Fe-labeled dinitrosyl iron compounds starting from ^{57}Fe metal.

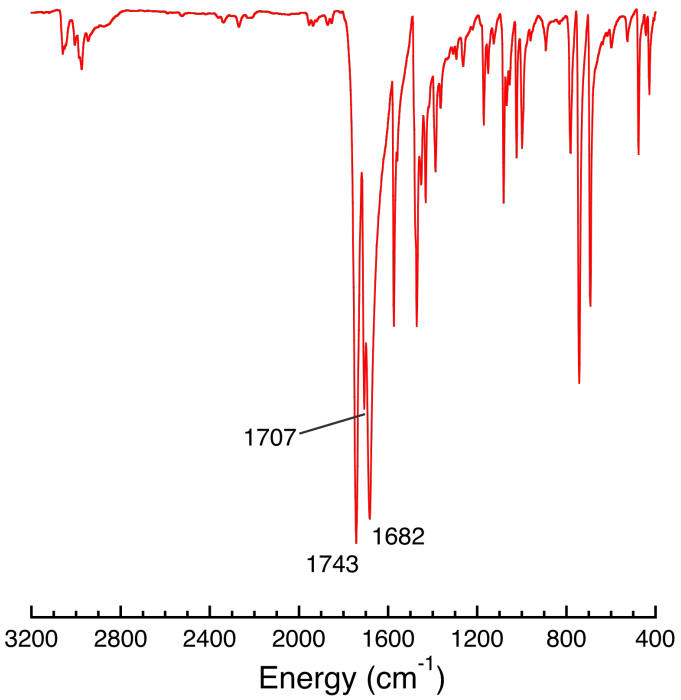

Figure S2. IR spectrum of $(Et_4N)[^{57}Fe(NO)_2(SPh)_2]$ as a KBr pellet.

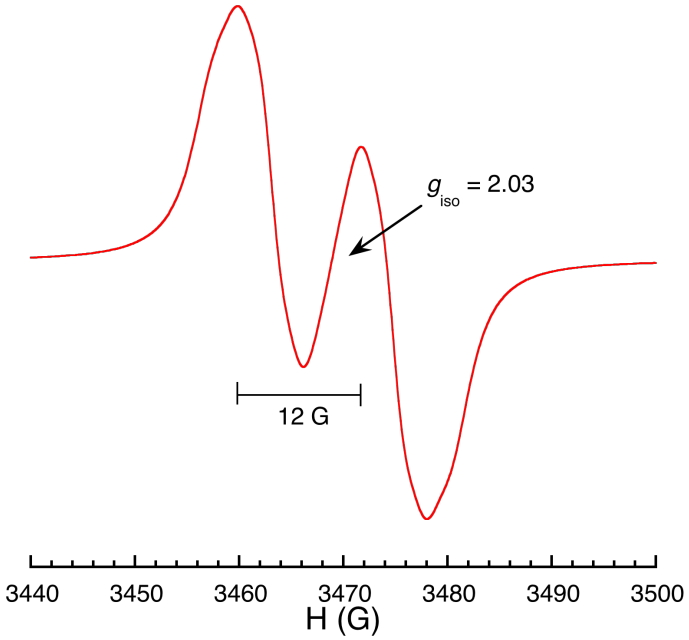

Figure S3. X-Band EPR spectrum of $(Et_4N)[^{57}Fe(NO)_2(SPh)_2]$ in THF at 295 K.

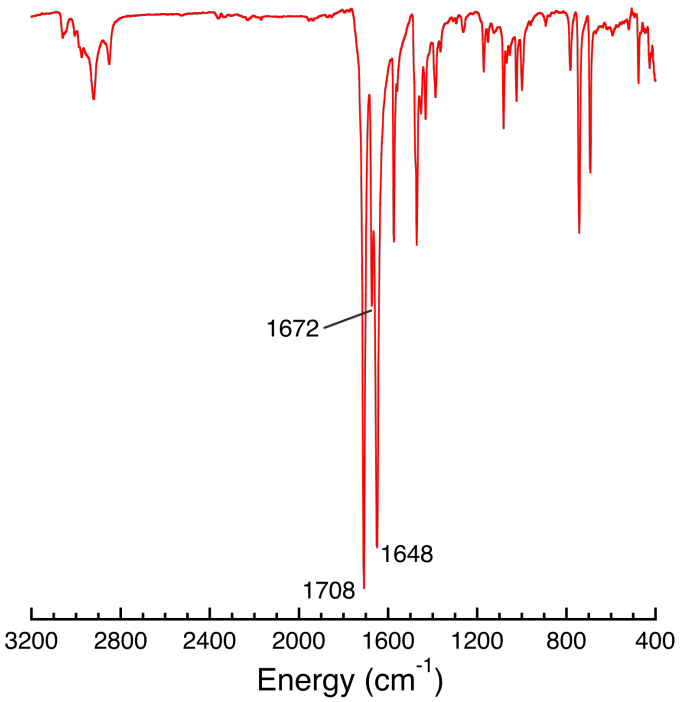

Figure S4. IR spectrum of $(Et_4N)[^{57}Fe(^{15}NO)_2(SPh)_2]$ as a KBr pellet.

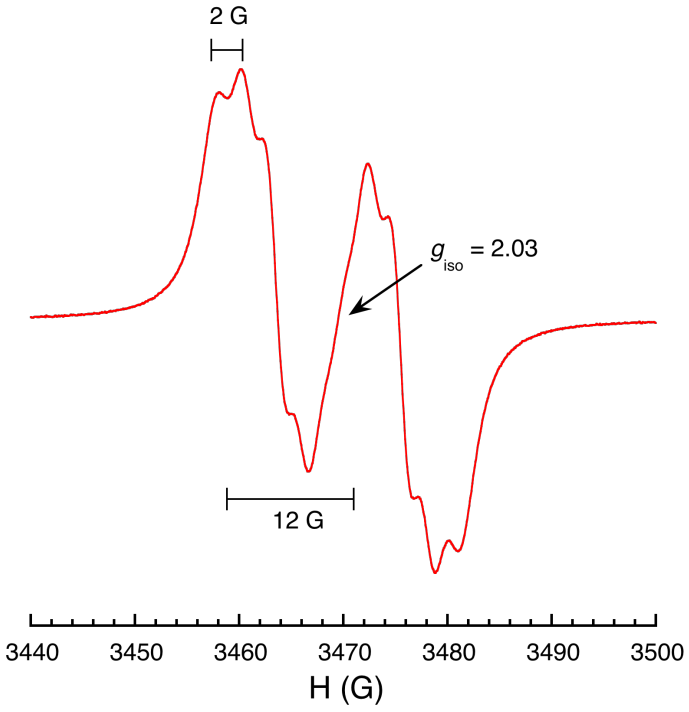

Figure S5. X-Band EPR spectrum of $(Et_4N)[^{57}Fe(^{15}NO)_2(SPh)_2]$ in THF at 295 K.

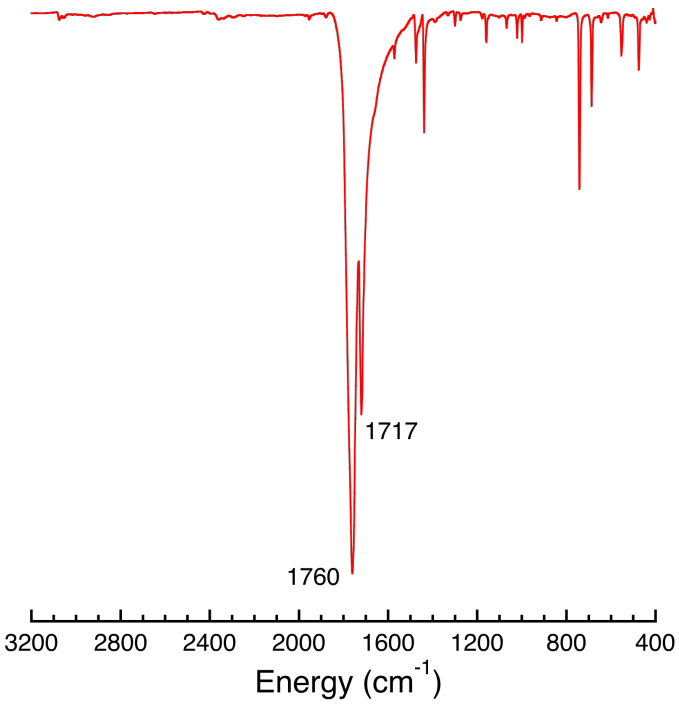

Figure S6. IR spectrum of [$^{57}Fe_2(\mu\text{-}SPh)_2(NO)_4$] as a KBr pellet.

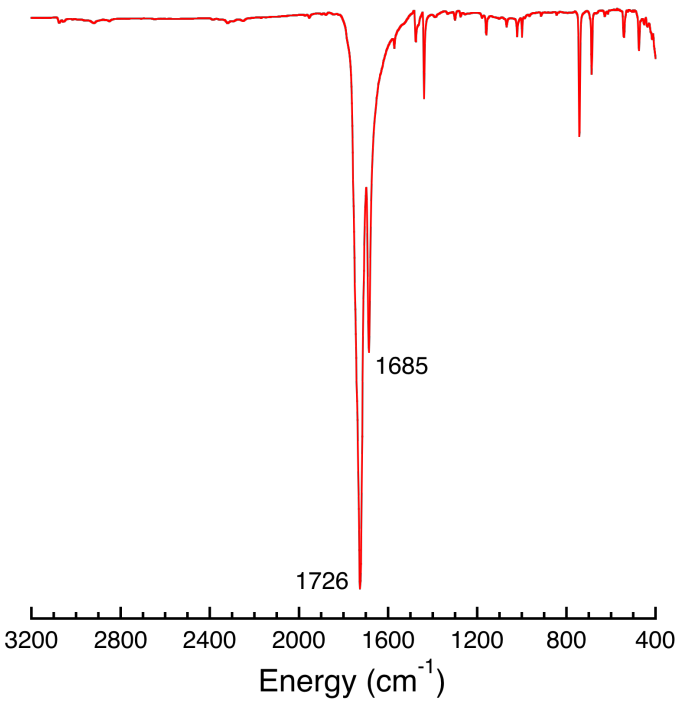

Figure S7. IR spectrum of [$^{57}Fe_2(\mu\text{-}SPh)_2(^{15}NO)_4$] as a KBr pellet.

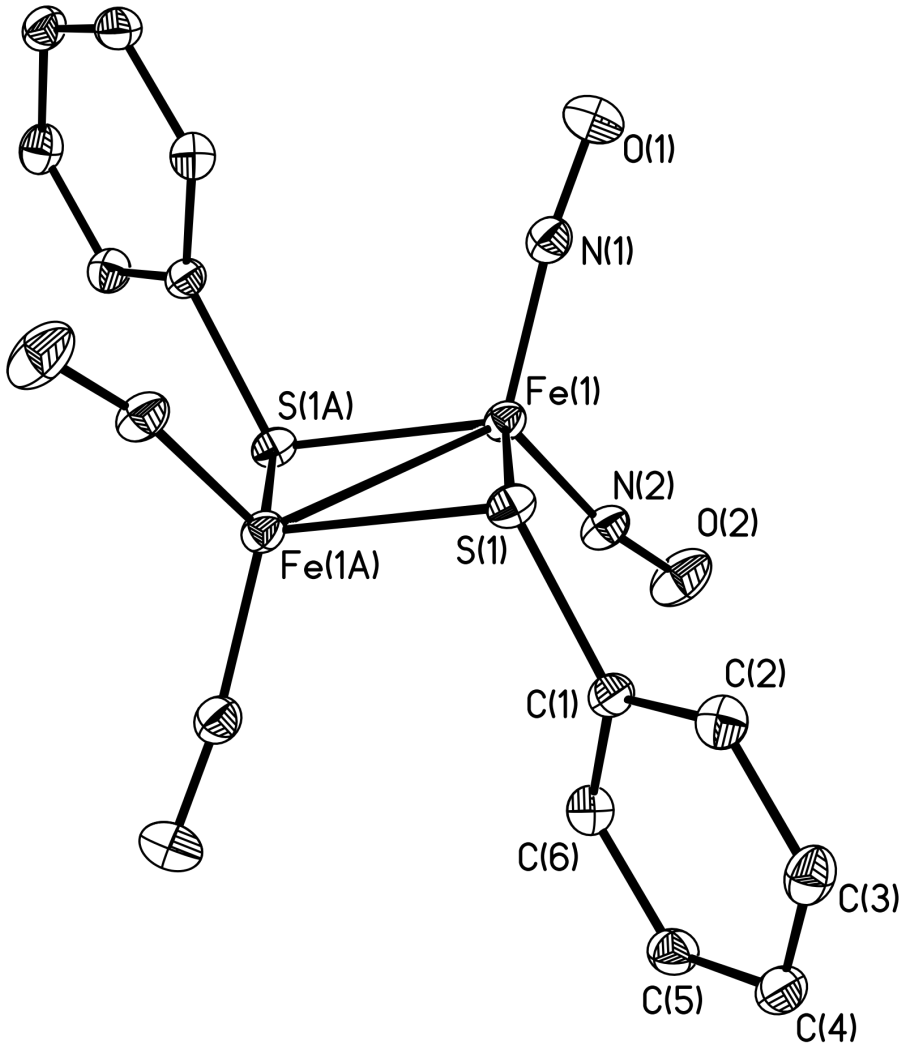

Figure S8. Thermal ellipsoid (50%) rendering of $[Fe_2(\mu\text{-}SPh)_2(NO)_4]$. Hydrogen atoms are omitted for clarity. Symmetry equivalent atoms other than Fe(1A) and S(1A) are unlabeled.

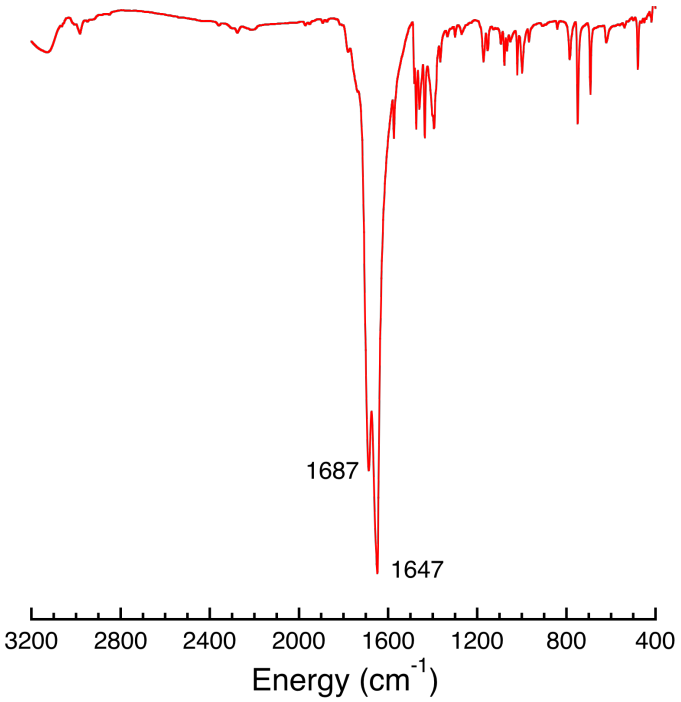

Figure S9. IR spectrum of $(Et_4N)[^{57}Fe_2(\mu\text{-}SPh)_2(NO)_4]$ as a KBr pellet.

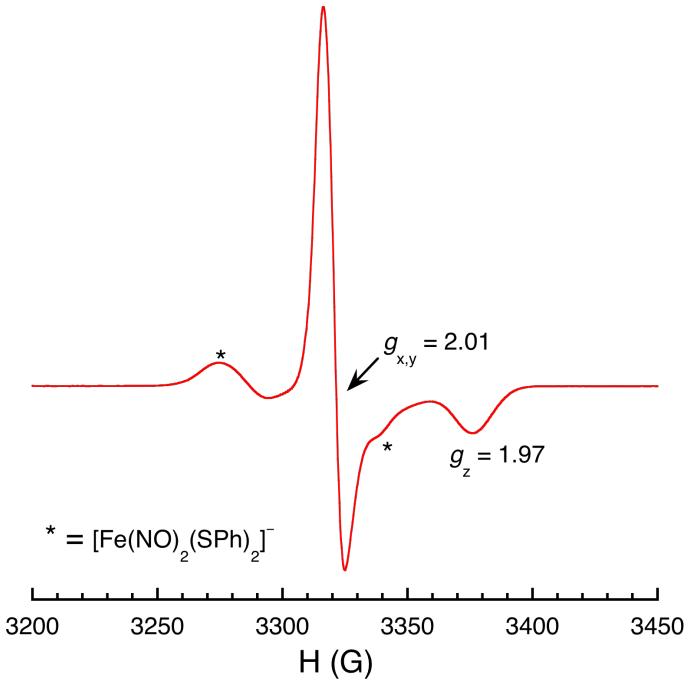

Figure S10. X-Band EPR spectrum of $(Et_4N)[Fe_2(\mu\text{-}SPh)_2(NO)_4]$ at 77 K in 2-MeTHF (~1 mM). Asterisks denote the $(Et_4N)[Fe(NO)_2(SPh)_2]$ impurity.

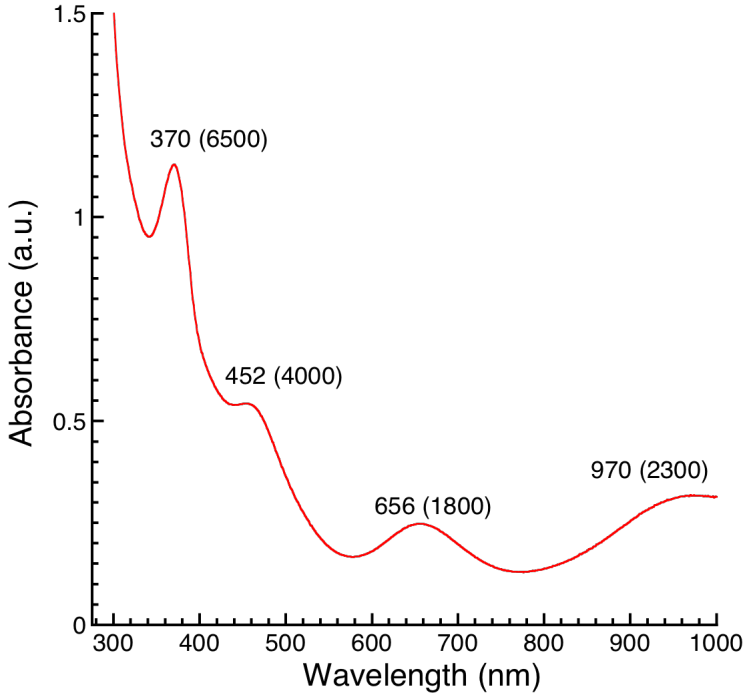

Figure S11. UV-vis spectrum of $(Et_4N)[Fe_2(\mu\text{-}SPh)_2(NO)_4]$ in THF (136 μM).

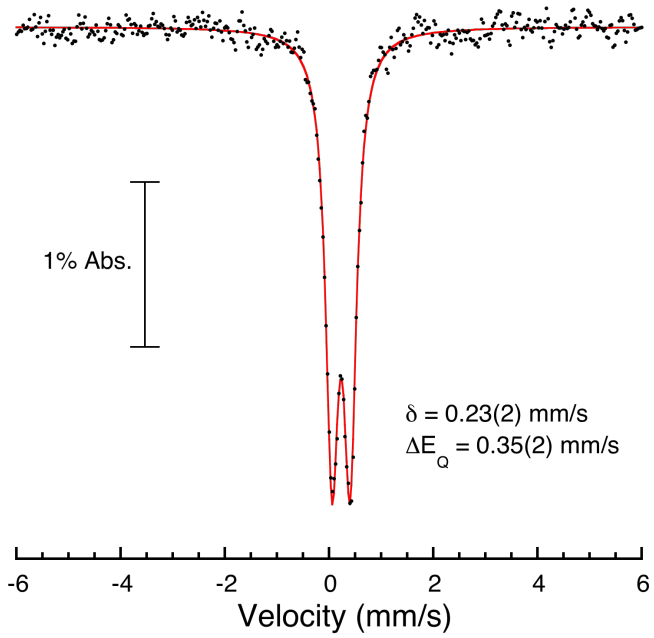

Figure S12. ^{57}Fe Mössbauer spectrum of polycrystalline $(Et_4N)[Fe_2(\mu\text{-}SPh)_2(NO)_4]$ at 90 K.

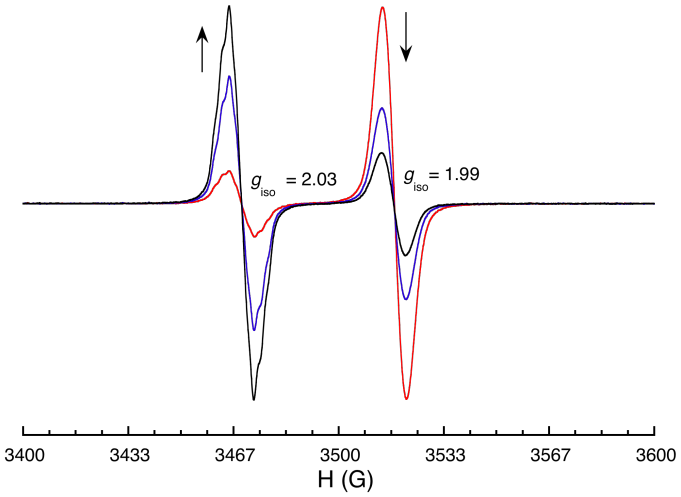

Figure S13. EPR spectral changes associated with the spontaneous conversion of $(Et_4N)[Fe_2(\mu\text{-}SPh)_2(NO)_4]$ (g = 1.99) to $(Et_4N)[Fe(NO)_2(SPh)_2]$ (g = 2.03) upon standing at 295 K in 2-MeTHF (~1 mM). Spectra are of recrystallized material after 10 min. (**red**), 24 h (**blue**), and 90 h (**black**) in solution.

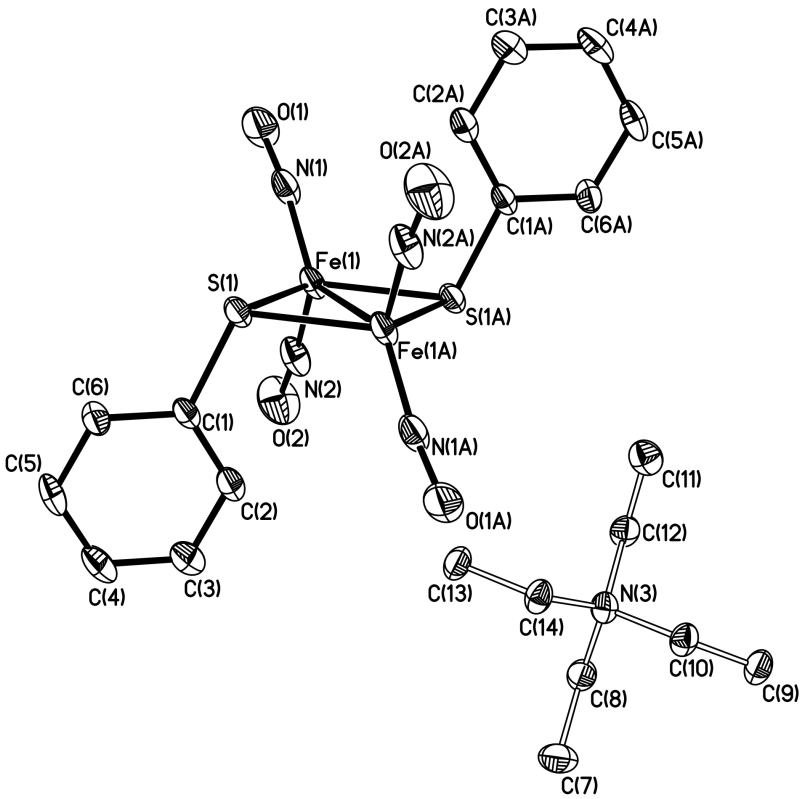

Figure S14. Thermal ellipsoid (50%) rendering of $(Et_4N)[Fe_2(\mu\text{-}SPh)_2(NO)_4]$. Hydrogen atoms and the minor component of the disordered Et_4N^+ cation are omitted for clarity.

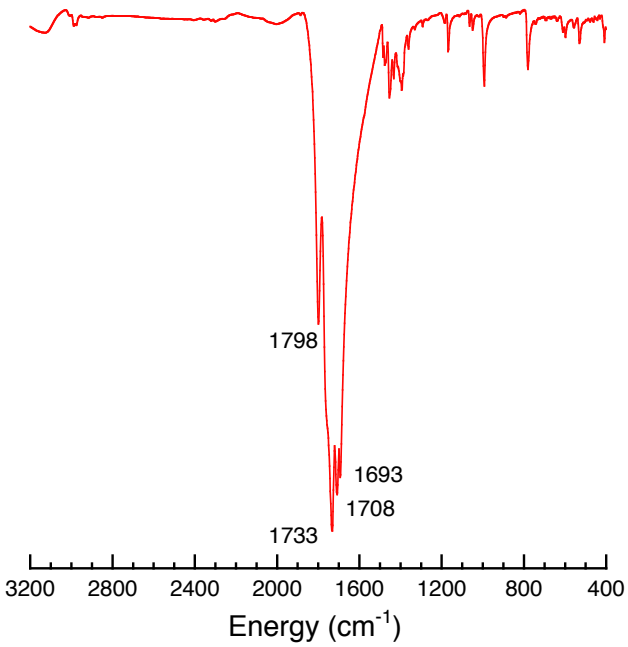

Figure S15. IR spectrum of $(Et_4N)[^{57}Fe_4(\mu_3\text{-}S)_3(NO)_7]$ as a KBr pellet.

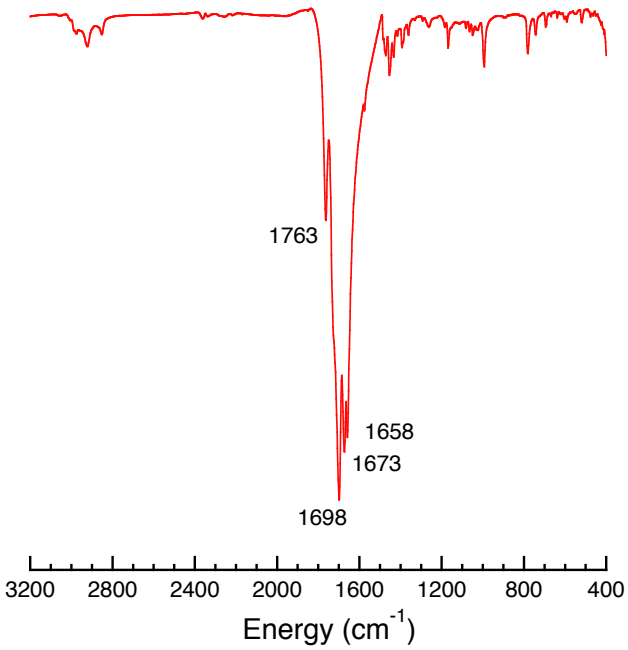

Figure S16. IR spectrum of $(Et_4N)[^{57}Fe_4(\mu_3\text{-}S)_3(^{15}NO)_7]$ as a KBr pellet.

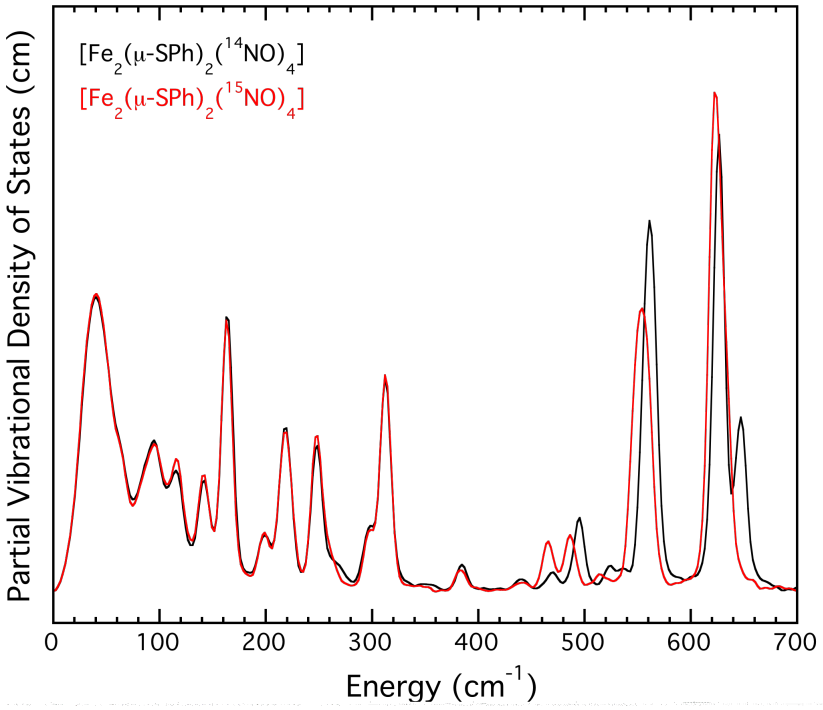

Figure S17. ^{57}Fe PVDOS of [$^{57}Fe_2(\mu\text{-}SPh)_2(^{14/15}NO)_4$].

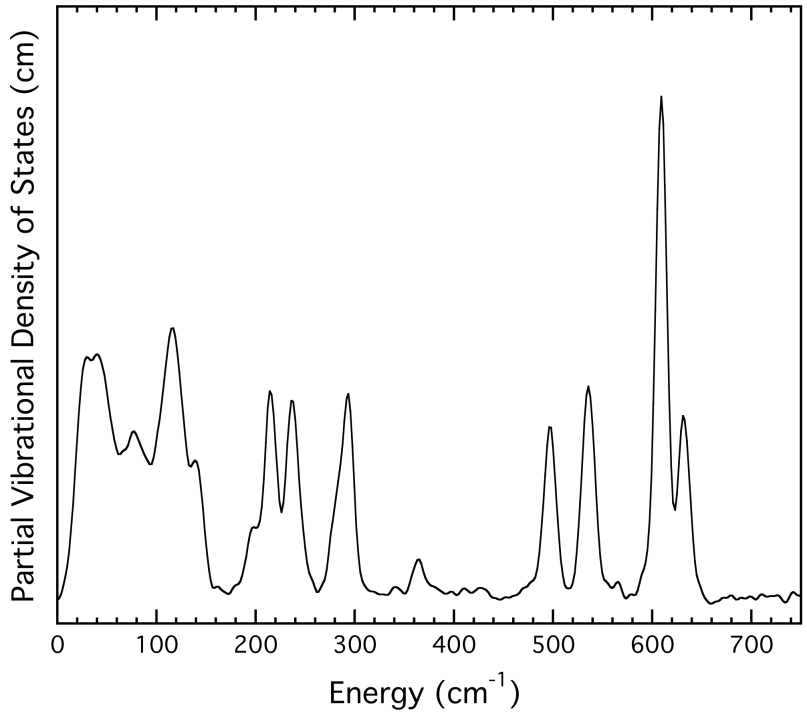

Figure S18. ^{57}Fe PVDOS of (Et_4N)[$^{57}Fe_2(\mu\text{-}SPh)_2(^{14}NO)_4$].

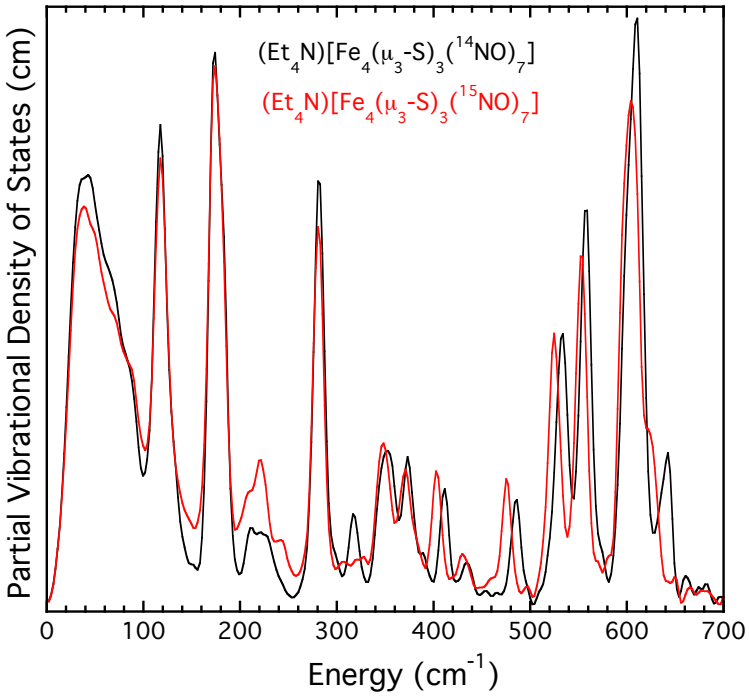

Figure S19. ^{57}Fe PVDOS of [$^{57}Fe_4(\mu_3\text{-}S)_3(^{14/15}NO)_7$].

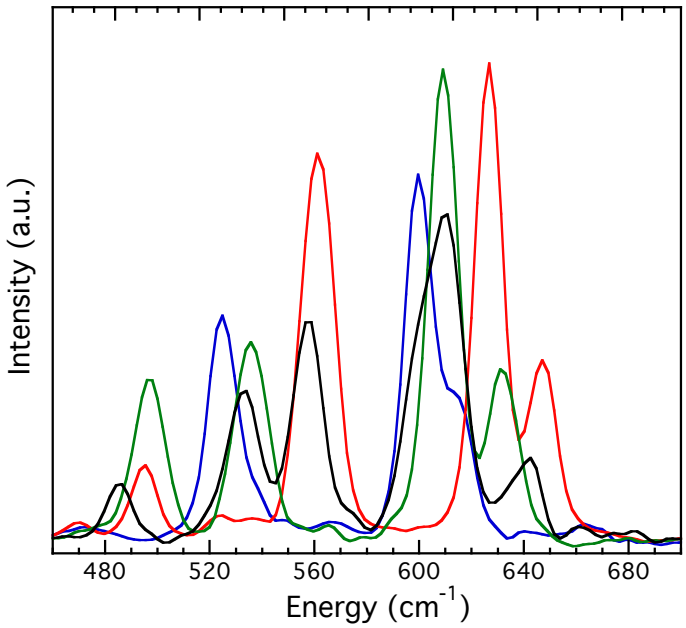

Figure S20. Overlay of the Fe-N(O) regions of the NRVS spectra for $(Et_4N)[^{57}Fe(NO)_2(SPh)_2]$ (**DNIC**), $[^{57}Fe_2(\mu\text{-}SPh)_2(NO)_4]$ (**RRE**), $(Et_4N)[^{57}Fe_4(\mu_3\text{-}S)_3(NO)_7]$ (**RBS**), and $(Et_4N)[^{57}Fe_2(\mu\text{-}SPh)_2(NO)_4]$ (**rRRE**).

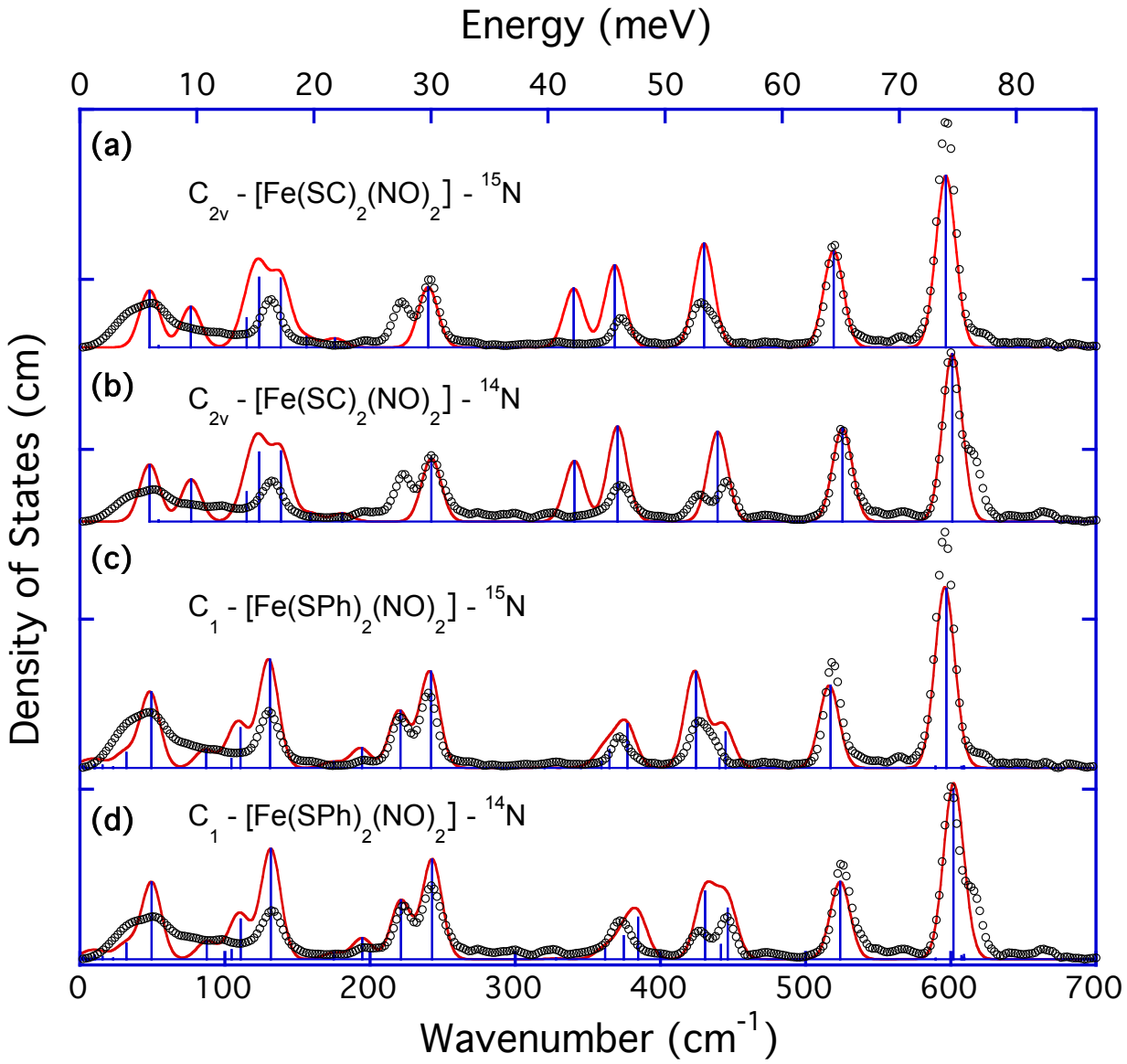

Figure S21. Urey-Bradley force field simulations (—) *vs*. experimental PVDOS (°°°) for $(Et_4N)[^{57}Fe(^{14/15}NO)_2(SPh)_2]$. Top to bottom: (a) $(Et_4N)[^{57}Fe(^{15}NO)_2(SPh)_2]$ *vs*. $[^{57}Fe(SC)_2(^{15}NO)_2]$ model in C_{2v} symmetry; (b) $(Et_4N)[^{57}Fe(^{14}NO)_2(SPh)_2]$ *vs*. $[^{57}Fe(SC)_2(^{14}NO)_2]$ model in C_{2v} symmetry; (c) $(Et_4N)[^{57}Fe(^{15}NO)_2(SPh)_2]$ *vs*. $[^{57}Fe(SPh)_2(^{15}NO)_2]$ model in C_1 symmetry; (d) $(Et_4N)[^{57}Fe(^{14}NO)_2(SPh)_2]$ *vs*. $[^{57}Fe(SPh)_2(^{14}NO)_2]$ model in C_1 symmetry. Sticks correspond to individual eigenmode frequencies and intensities before broadening.

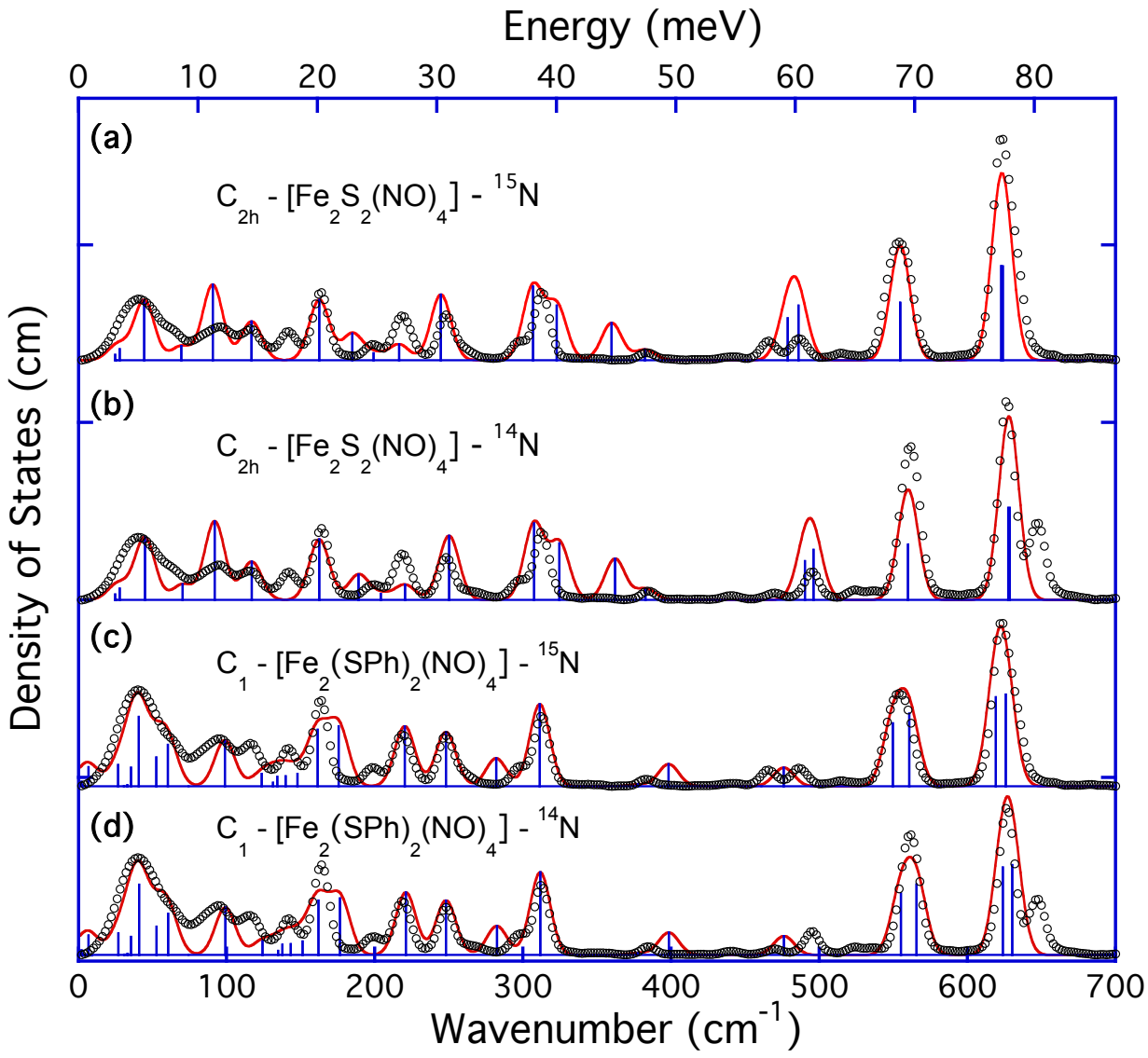

Figure S22. Urey-Bradley force field simulations (—) *vs.* experimental PVDOS (ººº) for [$^{57}Fe_2$(μ-SPh)$_2$($^{14/15}$NO)$_4$]. Top to bottom: (a) [$^{57}Fe_2$(μ-SPh)$_2$(^{15}NO)$_4$] *vs.* [$^{57}Fe_2S_2$(^{15}NO)$_4$] model in C_{2h} symmetry; (b) [$^{57}Fe_2$(μ-SPh)$_2$(^{14}NO)$_4$] *vs.* [$^{57}Fe_2S_2$(^{14}NO)$_4$] model in C_{2h} symmetry; (c) [$^{57}Fe_2$(μ-SPh)$_2$(^{15}NO)$_4$] *vs.* [$^{57}Fe_2$(SPh)$_2$(^{15}NO)$_4$] model in C_1 symmetry; (d) [$^{57}Fe_2$(μ-SPh)$_2$(^{14}NO)$_4$] *vs.* [$^{57}Fe_2$(SPh)$_2$(^{14}NO)$_4$] model in C_1 symmetry. Sticks correspond to individual eigenmode frequencies and intensities before broadening.

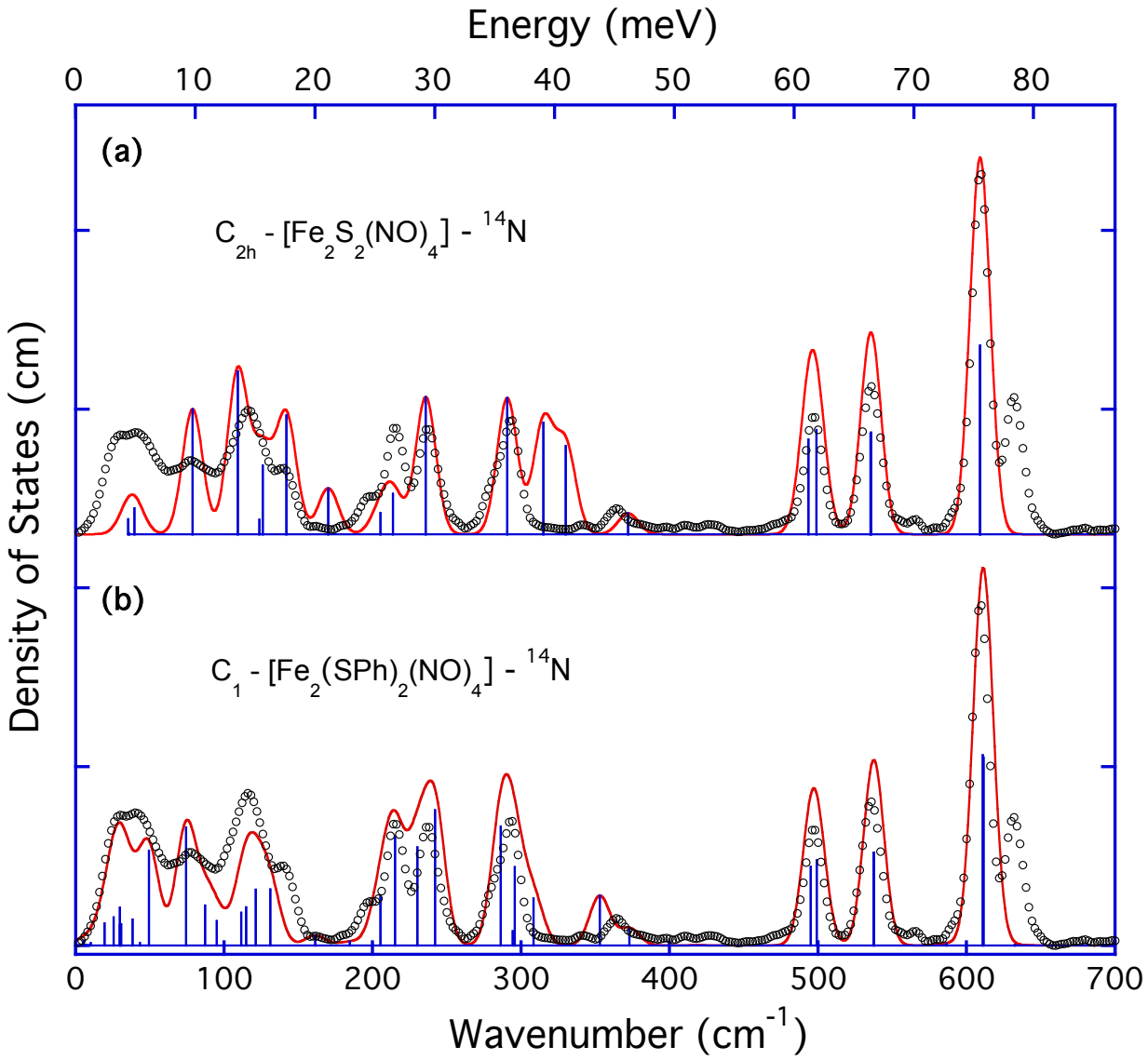

Figure S23. Urey-Bradley force field simulations (—) *vs*. experimental PVDOS (°°°) for $(Et_4N)[^{57}Fe_2(\mu\text{-}SPh)_2(^{14}NO)_4]$. Top to bottom: (a) $(Et_4N)[^{57}Fe_2(\mu\text{-}SPh)_2(^{14}NO)_4]$ *vs*. $[^{57}Fe_2S_2(^{14}NO)_4]$ model in C_{2h} symmetry; (b) $(Et_4N)[^{57}Fe_2(\mu\text{-}SPh)_2(^{14}NO)_4]$ *vs*. $[^{57}Fe_2(SPh)_2(^{14}NO)_4]$ model in C_1 symmetry. Sticks correspond to individual eigenmode frequencies and intensities before broadening.

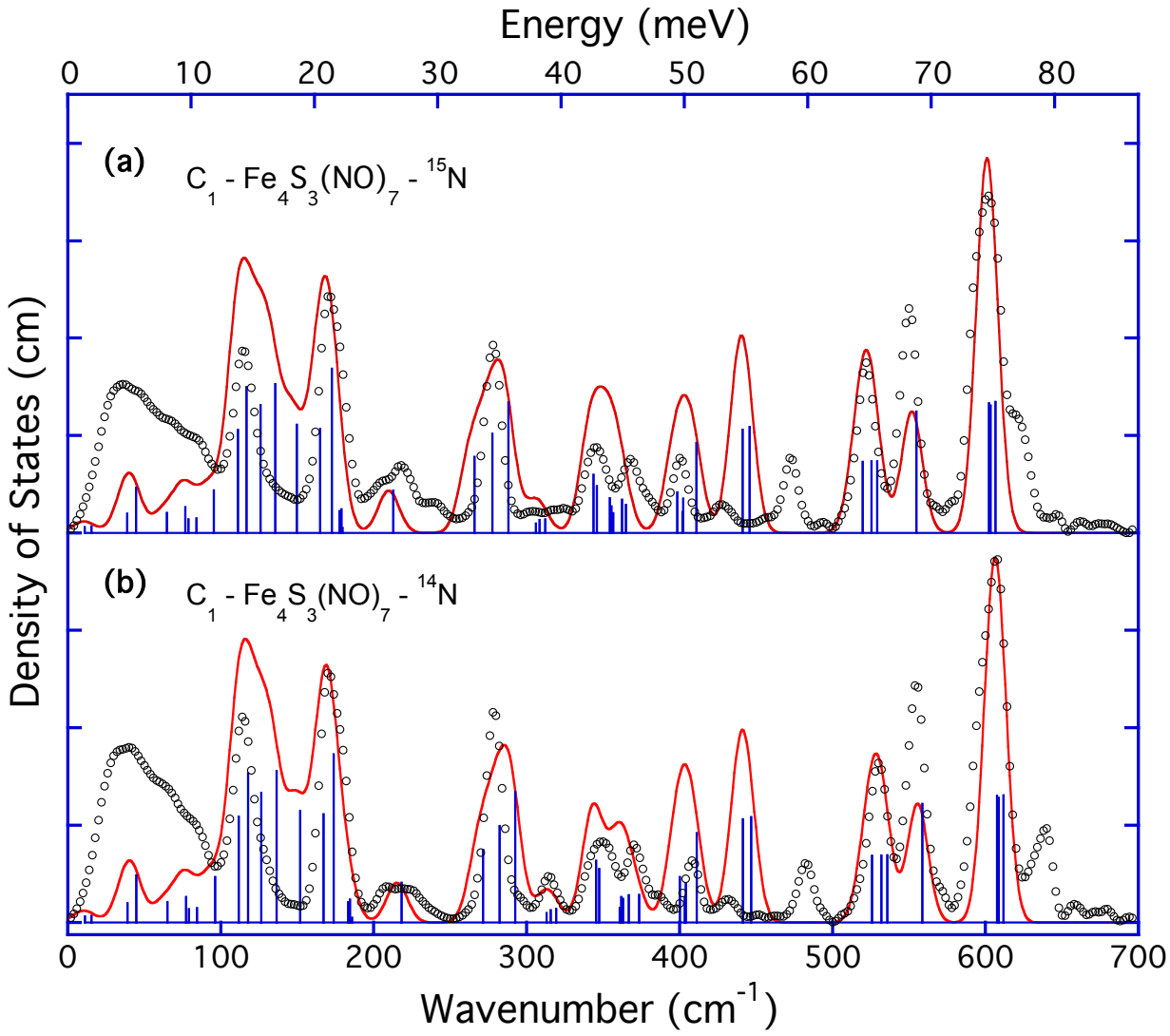

Figure S24. Urey-Bradley force field simulations (—) *vs*. experimental PVDOS (°°°) for $(Et_4N)[^{57}Fe_4(\mu_3\text{-}S)_3(^{14/15}NO)_7]$. Top to bottom: (a) $(Et_4N)[^{57}Fe_4(\mu_3\text{-}S)_3(^{15}NO)_7]$ *vs*. $[Fe_4S_3(^{15}NO)_7]$ model in C_1 symmetry; (b) $(Et_4N)[^{57}Fe_4(\mu_3\text{-}S)_3(^{14}NO)_7]$ *vs*. $[^{57}Fe_4S_3(^{14}NO)_7]$ model in C_1 symmetry. Sticks correspond to individual eigenmode frequencies and intensities before broadening.

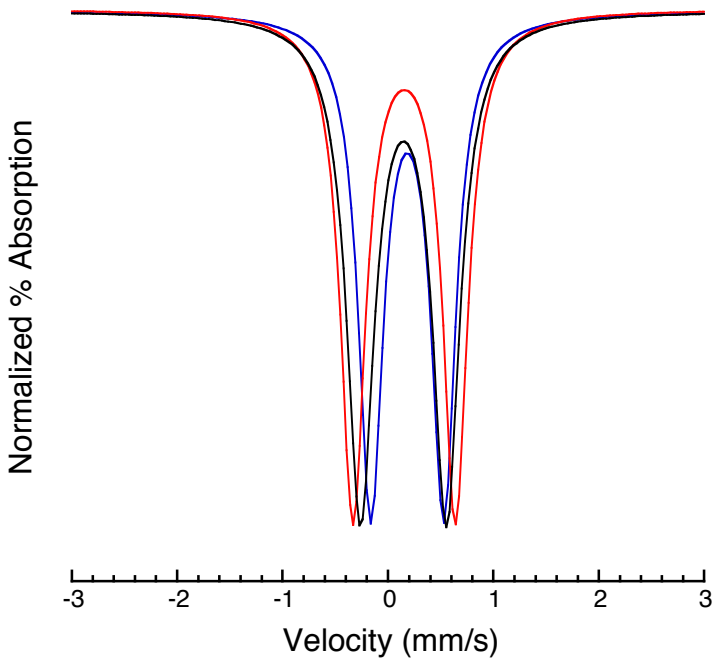

Figure S25. Overlay of the fits for ^{57}Fe Mössbauer data of $(Et_4N)[Fe(NO)_2(SPh)_2]$ (black), $[Fe_2(\mu\text{-}SPh)_2(NO)_4]$ (red), and $(Et_4N)[Fe_2(\mu\text{-}SPh)_2(NO)_4]$ (blue). Fits for each species are based on data recorded for polycrystalline samples at 90 K in the absence of an applied magnetic field.

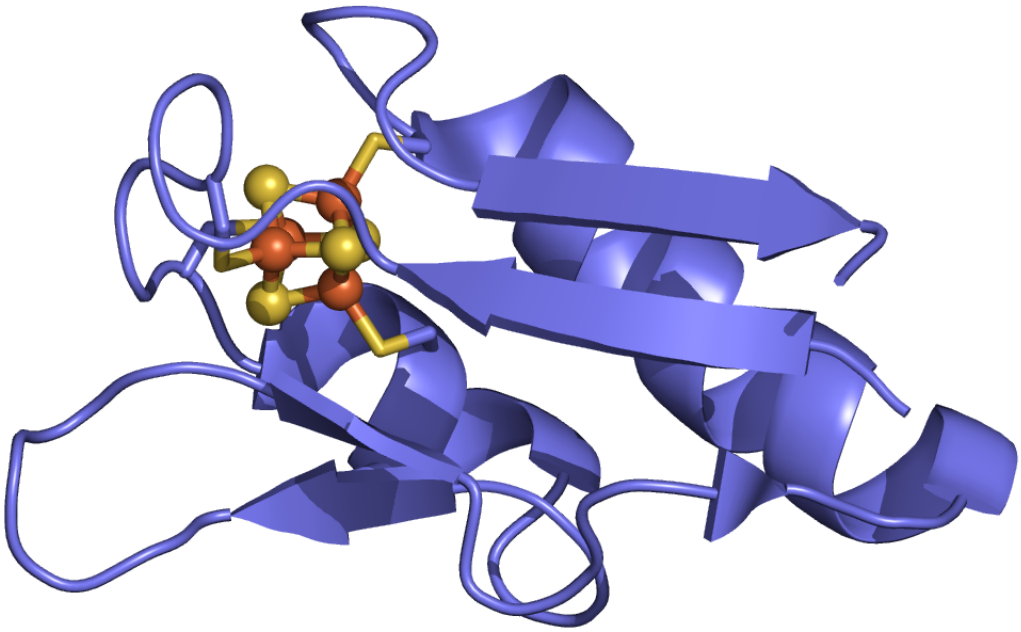

Figure S26. Structure of *P. furiosus* Fd D14C drawn with coordinates taken from the PDB, code 2Z8Q. Iron and selected sulfur atoms are colored orange and yellow, respectively.

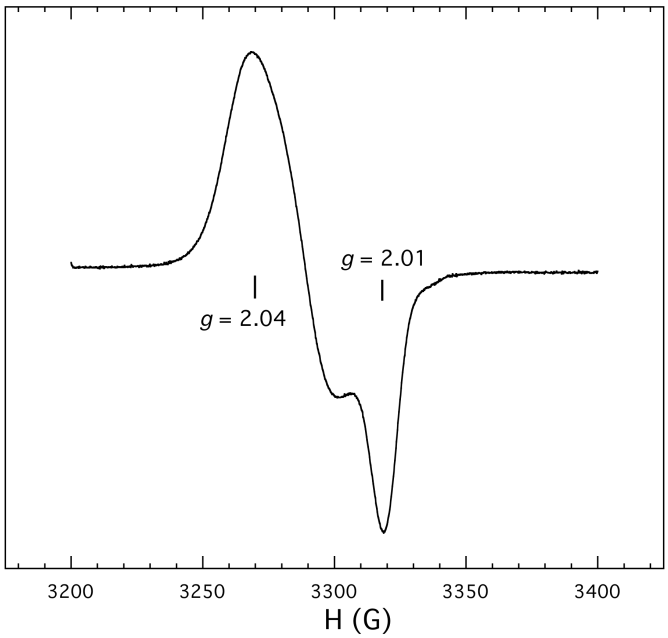

Figure S27. X-Band (9.35 GHz) EPR spectrum of the reaction of *P. furiosus* Fd D14C (760 µM) with PAPA NONOate recorded at 77 K. Conditions: 2.0 mW microwave power, 100.0 kHz modulation frequency, 8.00 G modulation amplitude.

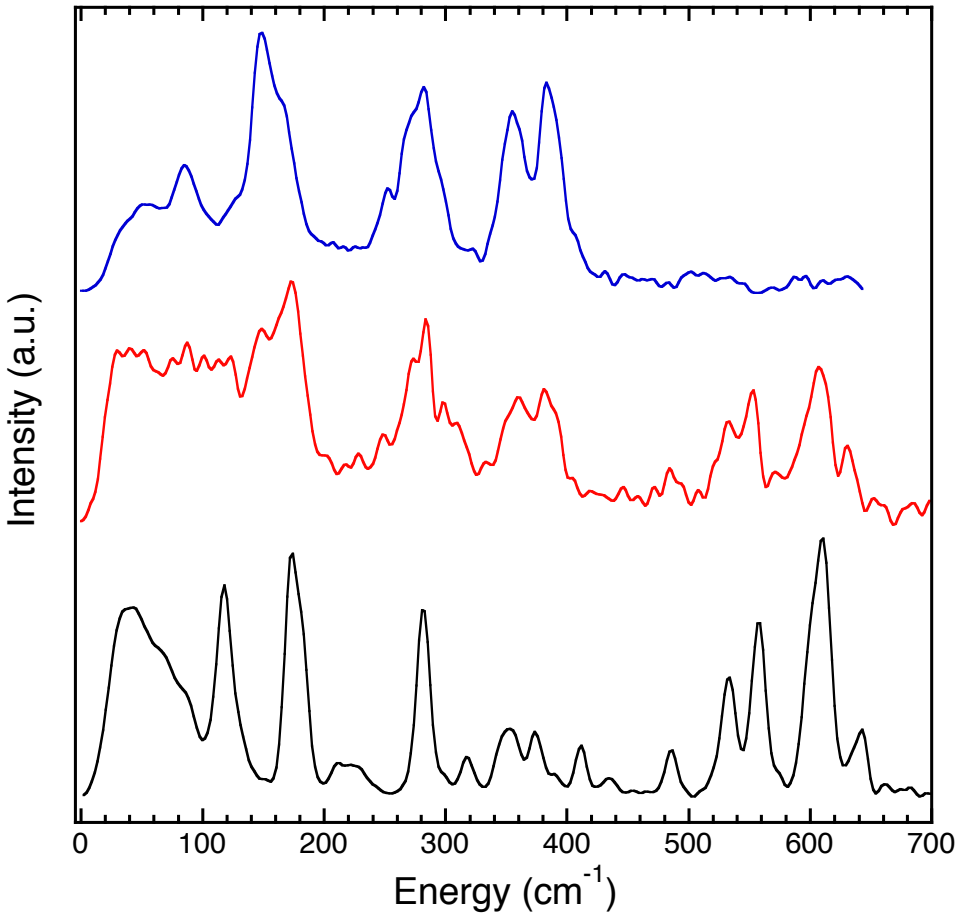

Figure S28. Overlay of the NRVS spectra for untreated *P. furiosus* Fd D14C (**top**), PAPA NONOate treated *P. furiosus* Fd D14C (**middle**) and $(Et_4N)[Fe_4(\mu_3\text{-}S)_3(NO)_7]$ (**bottom**).

References

(1) Pangborn, A. B.; Giardello, M. A.; Grubbs, R. H.; Rosen, R. K.; Timmers, F. J. *Organometallics* **1996**, *15*, 1518-1520.
(2) Lim, M. D.; Lorković, I. M.; Ford, P. C. In *Methods Enzymol.*; Academic Press: 2005; Vol. Volume 396, p 3-17.
(3) Kent, T. A. *WMOSS* v. 2.5: Mössbauer Spectral Analysis Software, WEB Research Co.; Minneapolis, MN, 1998.
(4) Hagen, K. S.; Reynolds, J. G.; Holm, R. H. *J. Am. Chem. Soc.* **1981**, *103*, 4054-4063.
(5) Hagen, K. S. *Inorg. Chem.* **2000**, *39*, 5867-5869.
(6) Harrop, T. C.; Tonzetich, Z. J.; Reisner, E.; Lippard, S. J. *J. Am. Chem. Soc.* **2008**, *130*, 15602-15610.
(7) Harrop, T. C.; Song, D.; Lippard, S. J. *J. Inorg. Biochem.* **2007**, *101*, 1730-1738.
(8) Brereton, P. S.; Verhagen, M. F. J. M.; Zhou, Z. H.; Adams, M. W. W. *Biochemistry* **1998**, *37*, 7351-7362.
(9) Menon, A. L.; Hendrix, H.; Hutchins, A.; Verhagen, M. F. J. M.; Adams, M. W. W. *Biochemistry* **1998**, *37*, 12838-12846.
(10) Sturhahn, W. *J. Phys.: Condens. Matter* **2004**, *16*, S497-S530.
(11) Dowty, E. *Phys. Chem. Miner.* **1987**, *14*, 67-79.
(12) Shape Software; http://www.shapesoftware.com/.
(13) Dai, R. J.; Ke, S. C. *J. Phys. Chem. B* **2007**, *111*, 2335-2346.
(14) Sheldrick, G. M. *Acta Crystallogr., Sect. A* **2008**, *A64*, 112-122.
(15) Sheldrick, G. M. *SADABS*: Area-Detector Absorption Correction; University of Göttingen: Göttingen, Germany, 2001.
(16) Spek, A. L. *PLATON*, A Multipurpose Crystallographic Tool; Utrecht University, Utrecht, The Netherlands, 2000.
(17) Sheldrick, G. M. *SHELXTL97*: Program for Refinement of Crystal Structures; University of Göttingen: Göttingen, Germany, 1997.
(18) Sedney, D.; Reiff, W. M. *Inorg. Chim. Acta* **1979**, *34*, 231-236.
(19) Hopmann, K. H.; Ghosh, A.; Noodleman, L. *Inorg. Chem.* **2009**, *48*, 9155-9165.